# ACADÉMIE DES SCIENCES
INSTITUT DE FRANCE

# *Comptes Rendus*

# *Physique*

Himanshu Patange, Kyrylo Gerashchenko, Rémi Rousseau, Paul Manset, Léo Balembois, Thibault Capelle, Samuel Deléglise and Thibaut Jacqmin

**Cryogenic rf-to-microwave transducer based on a dc-biased electromechanical system**

CENTRE
MERSENNE

ACADÉMIE
DES SCIENCES
INSTITUT DE FRANCE

Research article

# Cryogenic rf-to-microwave transducer based on a dc-biased electromechanical system

**Himanshu Patange** [a], **Kyrylo Gerashchenko** [a], **Rémi Rousseau** [a,b], **Paul Manset** [a], **Léo Balembois** [a], **Thibault Capelle** [c,d], **Samuel Deléglise** [#,a] and **Thibaut Jacqmin** [*,#,a,e]

[a] Laboratoire Kastler Brossel, Sorbonne Université, CNRS, ENS-Université PSL, Collège de France, 4 place Jussieu, 75005 Paris, France

[b] Alice & Bob, 53 Bd du Général Martial Valin, 75015 Paris, France

[c] Niels Bohr Institute, University of Copenhagen, Blegdamsvej 17, 2100 Copenhagen, Denmark

[d] Center for Hybrid Quantum Networks (Hy-Q), Niels Bohr Institute, University of Copenhagen, Copenhagen, Denmark

[e] Institut Universitaire de France (IUF), 1 rue Descartes, 75231 Paris, France

*E-mail:* thibaut.jacqmin@lkb.upmc.fr

**Abstract.** We report a two-stage, heterodyne rf-to-microwave transducer that combines a tunable electrostatic pre-amplifier with a superconducting electromechanical cavity. A metalized $Si_3N_4$ membrane (3 MHz frequency) forms the movable plate of a vacuum-gap capacitor in a microwave LC resonator. A dc bias across the gap converts any small rf signal into a resonant electrostatic force proportional to the bias, providing a voltage-controlled gain that multiplies the cavity's intrinsic electromechanical gain. In a flip-chip device with a 1.5 μm gap operated at 10 mK we observe dc-tunable anti-spring shifts, and rf-to-microwave transduction at 49 V bias, achieving a charge sensitivity of 87 μe/$\sqrt{Hz}$ (0.9 nV/$\sqrt{Hz}$). Extrapolation to sub-micron gaps and state-of-the-art $Q > 10^8$ membrane resonators predicts sub-200 fV/$\sqrt{Hz}$ sensitivity, establishing dc-biased electromechanics as a practical route towards quantum-grade rf electrometers and low-noise modular heterodyne links for superconducting microwave circuits and charge or voltage sensing.

[#]Contributed equally

[*]Corresponding author

## 1. Introduction

Bridging the gap between radio-frequency (rf) and microwave-frequency electrical signals is a longstanding challenge in quantum electronics and precision sensing. If an rf signal can be upconverted without adding noise, it can be processed by near-quantum-limited amplifiers that are available in the microwave frequency band. In a typical electro-mechanical transducer, an rf charge modulation drives a mechanical mode into motion. The motion is then converted into a microwave sideband that can be measured with sub-nV/$\sqrt{\text{Hz}}$ sensitivity. Such a device can also be used as a sensitive electrometer.
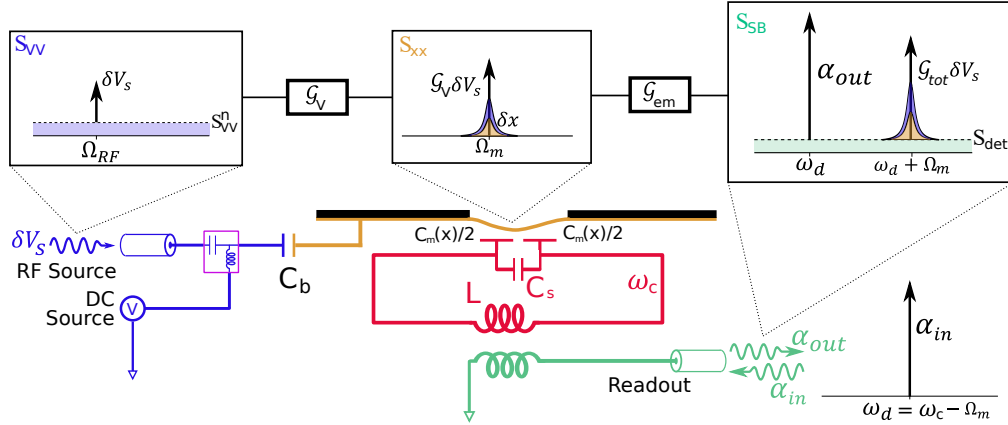


**Figure 1.** Top: illustration of the transducer amplification chain, where the electrical spectrum $S_{\text{VV}}$ (signal $\delta V_s$ at frequency $\Omega_{\text{RF}}$ plus white noise of spectral density $S_{\text{VV}}^n$, indicated in purple) undergoes transduction to position spectrum $S_{\text{xx}}$ with the electrostatic gain $\mathcal{G}_{\text{V}}$ (electrical noise contribution appears in purple, and thermal noise contribution in orange) followed by transduction to microwave sideband spectrum $S_{\text{SB}}$ via the electromechanical gain $\mathcal{G}_{\text{em}}$ (detection noise contribution is indicated in light green). Bottom: proposed implementation of the transducer. An LC microwave resonator (red) of resonance frequency $\omega_{\text{c}}$ is coupled to a metalized free standing membrane acting as a mechanically compliant capacitor. The red part of the circuit is electrically floating. The membrane electrode (yellow) is biased through a capacitor $C_{\text{b}}$, connected to a bias tee (pink rectangle) that combines the dc bias and an rf signal to drive membrane modes on resonance. The two halves of the membrane electrode behave as $C_m(x)/2$ capacitors that are connected in parallel with the microwave LC resonator, and in series with the bias-line, so that the bias circuit sees the full membrane capacitance $C_m(x)$ whereas the LC resonator sees only $C_m(x)/4$ in parallel with its stray capacitance $C_{\text{s}}$. The LC resonator is inductively coupled to a read-out line (green). A probe tone $\alpha_{\text{in}}$ at the red-detuned frequency $\omega_{\text{d}} = \omega_{\text{c}} - \Omega_{\text{m}}$ is sent into the resonator, and the reflected field $\alpha_{\text{out}}$ is monitored with a vector spectrum analyser. In this scheme, the mechanical mode of amplitude $\delta x$, is driven on resonance by the rf source, and amplified by the dc source with a gain $\mathcal{G}_V$. It is then upconverted and amplified with a gain $\mathcal{G}_{\text{em}}$ at microwave frequencies by the electromechanical system operating in the resolved sideband regime. It appears as a sideband of the reflected microwave carrier $\alpha_{\text{out}}$.

The seminal electrometer of Knobel and Cleland exploits a radio-frequency single-electron transistor to measure the motion of a suspended beam and achieves a charge sensitivity of 12 µe/$\sqrt{\text{Hz}}$ [1]. Subsequent transport-based devices — rf-SETs [2–7], rf-QPC [8], quantum dots [9–11], gate-based devices [12], and fluxonium qubits [13,14] — have pushed sensitivities below 10 µe/$\sqrt{\text{Hz}}$. A parallel track replaces the electronic detector with an optical or microwave cavity coupled to a high-Q mechanically compliant capacitor. In such schemes, one exploits the high susceptibility of the resonant mechanical system to probe an external force, such as an electrostatic modulation, with high sensitivity. Cavity-enhanced microwave read-out of a nanobeam was obtained at room temperature [15]. Additionally, ground-state cooling and imprecision at the standard quantum limit have been achieved in both microwave [16–18] and optical [19–22] domains, while ultracoherent $\text{Si}_3\text{N}_4$ membranes with $Q > 10^9$ [18,23–25] for

mechanical modes in the 100 kHz range, now suppress thermomechanical force noise to the zeptonewton level [18,24]. Meanwhile, cavity electro-optomechanical converters have linked microwave and optical photons [26–30].

In most cavity-based converters the microwave cavity alone supplies the gain. The linearized coupling grows with the intracavity photon number, so that achieving higher conversion efficiency requires strong pumps — at the cost of photon shot-noise or heating. Here we report on a two-stage architecture that sidesteps that trade-off by pre-amplifying the rf signal electrostatically before it reaches the cavity. More precisely, we propose a heterodyne rf-to-microwave converter based on a dc-biased membrane. It consists of a metalized $Si_3N_4$ membrane whose fundamental drum mode lies near 3 MHz. The membrane forms one plate of a vacuum-gap capacitor in a superconducting lumped-element LC resonator at 6 GHz, such that its motion modulates the microwave resonance frequency. A dc bias applied across the gap converts any small rf signal on the same line into a time-varying electrostatic force that scales linearly with the bias voltage [14,28,31,32]. This electrostatic stage adds a voltage-tunable pre-amplification to the RF signal before it is upconverted by the LC microwave resonator. Because the two stages act in series, their gains multiply, boosting the overall RF-to-microwave conversion. A related dc-biased membrane-based rf-to-optical transducer was demonstrated by Bagci et al. [28], where a sub-MHz rf voltage is converted to an optical carrier with a voltage sensitivity of a few $pV/\sqrt{Hz}$, and further experimental and theoretical developments along similar lines have been reported in [33,34]. In the present cryogenic implementation, we demonstrate a flip-chip assembly that realises a 1.5 μm vacuum gap, and observe dc-controlled frequency shifts on the mechanical modes — a static effect known as anti-spring effect [14,28,31]. With a 49 V bias, the device achieves a charge sensitivity of 87 $μe/\sqrt{Hz}$ (0.9 $nV/\sqrt{Hz}$), currently limited by bias-line noise. With sub-micrometer gaps and $Q > 10^8$ membranes already demonstrated [18,25,35], our model predicts that sub-200 $fV/\sqrt{Hz}$ sensitivity is within reach, paving the way towards quantum-grade rf electrometers and heterodyne links that integrate seamlessly with microwave quantum circuits.

## 2. Transduction principle

The proposed design, described in Figure 1, consists of a metalized membrane oscillator (mode frequency $\Omega_m/2\pi$ of a few MHz, and effective mass $m_{eff}$), dispersively coupled to a superconducting lumped-element LC resonator (frequency $\omega_c/2\pi$ of a few GHz). The capacitance of the LC resonator consists of a stray capacitance $C_s$ in parallel with two mechanically compliant vacuum gap capacitance $C_m(x)/2$ in series. The metalized membrane constitutes one plate of each capacitor $C_m(x)/2$, such that its out-of-plane motion $x(t)$ shifts $\omega_c$ according to $\omega_c(x) = \left(L(C_m(x)/4 + C_s)\right)^{-1/2}$. To first order, this leads to a modulation of the microwave resonator frequency $\delta\omega_c(t) = (\partial_x\omega_c)x(t)$. The LC resonator is weakly coupled to a read-out line and probed in reflection. A coherent microwave tone is applied with a frequency $\omega_d$ typically red-detuned by one mechanical frequency: $\omega_d \approx \omega_c - \Omega_m$. In the linear regime, the reflected field acquires sidebands [36] at $\omega_d \pm \Omega_m$, with a power spectral density expressed in $V^2/Hz$

$$S_{SB}[\omega] = \mathcal{G}_{em}^2(\omega)S_{xx}[\omega], \tag{1}$$

where $S_{xx}[\omega]$ is the power spectrum of the membrane position, and $\mathcal{G}_{em}(\omega)$ the electromechanical gain, which can be approximated by

$$\mathcal{G}_{em}(\omega) \simeq G\sqrt{n\kappa_c}|A_-(\omega)|\sqrt{\hbar\omega_c Z/2} \tag{2}$$

in the resolved sideband regime ($\Omega_m \gg \kappa$), with $n$ being the microwave mode photon number, $G = \partial_x\omega_c$ the electromechanical coupling strength, $A_-(\omega) = \left[-i(\Delta + \omega) + \kappa/2\right]^{-1}$ the microwave resonator response at detuning $\Delta = \omega_d - \omega_c$, and $Z$ is the read-out line characteristic impedance.

Here, we have introduced the microwave resonator linewidth $\kappa = \kappa_c + \kappa_i$, the coupling rate to the read-out line $\kappa_c$, and the intrinsic loss rate of the microwave mode $\kappa_i$. This electromechanical system is used to upconvert and amplify the motion of the mechanical oscillator to the microwave domain. This technique is the standard read-out protocol for microwave optomechanical systems [16,18].

In addition, we add a static bias voltage $V$ and a small rf sinusoidal modulation $\delta V(t)$ on the membrane electrode through an external bias capacitor $C_{\mathrm{b}}$ (see Figure 1). Because $C_{\mathrm{b}}$ is in series with $C_{\mathrm{m}}$, the two capacitors can be replaced by the equivalent capacitance $C_{\mathrm{eq}} = (C_{\mathrm{m}}^{-1} + C_{\mathrm{b}}^{-1})^{-1}$. $V + \delta V(t)$ is applied across $C_{\mathrm{eq}}$, so that only the fraction $\eta(V + \delta V(t))$, with $\eta = C_{\mathrm{b}}/(C_{\mathrm{b}} + C_{\mathrm{m}})$ drops across the mechanical capacitor $C_{\mathrm{m}}(x)$, the factor $\eta$ acting as a voltage dilution coefficient. The electrostatic potential energy of the system writes $U(x,t) = -C_{\mathrm{eq}}(x)[V + \delta V(t)]^2/2$. Expanding to first order in $\delta V/V$ yields the force

$$F_{\mathrm{el}}(t) \equiv -\partial_x U \simeq \frac{1}{2} V^2 \partial_x C_{\mathrm{eq}} + V \delta V(t) \partial_x C_{\mathrm{eq}}. \tag{3}$$

The first term is a static electrostatic force that both softens the membrane spring — producing the familiar anti-spring frequency shift [14,28,31,37,38] $\Omega_{\mathrm{m}}^2(V) = \Omega_{\mathrm{m}}^2(0) - V^2 \partial_x^2 C_{\mathrm{eq}}/2$ — and increases the mechanical linewidth through motion-induced currents in any resistive elements $R$ of the biasing circuit, with the bias-dependent damping $\Gamma_{\mathrm{m}}(V) = \Gamma_{\mathrm{m}}(0) + V^2(\partial_x^2 C_{\mathrm{eq}})^2 R/m_{\mathrm{eff}}$ (detailed calculations can be found in [39]). The second term drives the membrane motion, with a force scaling linearly with $V$. The mechanical mode response to $F_{\mathrm{el}}(t)$ is given by an effective voltage-dependent mechanical susceptibility $\chi_{\mathrm{m}}(\omega, V)$ defined by

$$\chi_{\mathrm{m}}(\omega, V)^{-1} = m_{\mathrm{eff}}[\Omega_{\mathrm{m}}^2(V) - \omega^2 - i\omega\Gamma_{\mathrm{m}}(V)]. \tag{4}$$

Hence, an rf signal of spectrum $S_{\mathrm{VV}}[\omega]$ is transduced into displacement with the spectrum

$$S_{\mathrm{xx}}^{\mathrm{el}}[\omega] = \mathcal{G}_V(\omega)^2 S_{\mathrm{VV}}[\omega], \tag{5}$$

where we have introduced the electrostatic gain

$$\mathcal{G}_V(\omega) = |\chi_{\mathrm{m}}(\omega, V) V \partial_x C_{\mathrm{eq}}|, \tag{6}$$

which grows linearly with $V$ and peaks at $\omega = \Omega_m(V)$. The resulting overall transduction gain from an rf tone amplitude to a microwave sideband amplitude writes

$$\mathcal{G}_{\mathrm{tot}}(\omega) = \mathcal{G}_{\mathrm{em}}(\omega) \times \mathcal{G}_V(\omega). \tag{7}$$

The proposed device comprises two cascaded amplifiers: the electromechanical stage, whose gain $\mathcal{G}_{\mathrm{em}}$ depends on the microwave pump power and on the electromechanical coupling $G$, and the electrostatic stage, whose gain $\mathcal{G}_V$ can be tuned *in situ* by the dc bias $V$. This shows that such transducer can be used to upconvert to the microwave domain and amplify small rf voltage fluctuations. In the following, we perform a noise budget, compute an expression for the total transduction gain, and derive an ultimate sensitivity of such a system used as an electrometer or charge sensor.

## 3. Signal-to-noise ratio in an rf-to-microwave transduction experiment

Force and position noise spectra are related by the mechanical susceptibility

$$S_{\mathrm{xx}}[\omega] = |\chi_{\mathrm{m}}(\omega, V)|^2 S_{\mathrm{FF}}[\omega]. \tag{8}$$

Thermal force noise $S_{\mathrm{FF}}^{\mathrm{th}}$, electrical force noise $S_{\mathrm{FF}}^{\mathrm{el}}$ and cavity back-action force noise [36] $S_{\mathrm{FF}}^{\mathrm{ba}}$ contribute to the total force noise as

$$S_{\mathrm{FF}}[\omega] = S_{\mathrm{FF}}^{\mathrm{th}}[\omega] + S_{\mathrm{FF}}^{\mathrm{el}}[\omega] + S_{\mathrm{FF}}^{\mathrm{ba}}[\omega], \tag{9}$$

where

$$S_{FF}^{th}[\omega] = 2m_{eff}\Gamma_m k_B T \qquad (10)$$

is the Langevin thermal force noise, with $T$ the environmental temperature, and $S_{FF}^{el}[\omega] = \left(\mathcal{G}_V[\omega]/|\chi_m(\omega, V)|\right)^2 S_{VV}[\omega]$ the force noise due to direct electrical drive on the membrane electrode. Including both $S_{FF}[\omega]$ and the detection noise $S_{det}$, the transduced sideband spectrum writes

$$S_{SB}[\omega] = \mathcal{G}_{tot}^2(\omega)S_{VV}(\omega) + \mathcal{G}_{em}^2(\omega)|\chi_m(\omega, V)|^2(S_{FF}^{th} + S_{FF}^{ba}) + S_{det}, \qquad (11)$$

where the first term in the right-hand side is the term of interest. Splitting the input rf noise spectrum into signal and noise contributions as $S_{VV} = S_{VV}^s + S_{VV}^n$, we introduce the signal to noise ratio of the transduction experiment:

$$SNR^2 = \frac{\mathcal{G}_{tot}^2(\omega)S_{VV}^s}{\mathcal{G}_{tot}^2(\omega)S_{VV}^n + \mathcal{G}_{em}^2(\omega)|\chi_m(\omega, V)|^2(S_{FF}^{th} + S_{FF}^{ba}) + S_{det}}. \qquad (12)$$

Eq. (12) shows that the SNR can be improved by increasing the total transduction gain $\mathcal{G}_{tot}$ as long as the dominant noise in the denominator is not amplified by the same factor. The total gain is controlled by two parameters: the electrostatic pre-amplification set by the dc bias $V$ and the microwave stage set by the intracavity photon number $n$ through the linearized coupling $g_0\sqrt{n}$, with $g_0 = Gx_{zpf}$ the vacuum electromechanical coupling and $x_{zpf} = \sqrt{\hbar/2m_{eff}\Omega_m}$ the zero point fluctuations of position. In the low-cooperativity limit this yields the scaling $\mathcal{G}_{tot} \propto |V|\sqrt{n}$. Therefore, in the imprecision-limited regime (denominator dominated by $S_{det}$) one expects $SNR \propto |V|\sqrt{n}$. By contrast, when the transduced input electrical noise term $\mathcal{G}_{tot}^2 S_{VV}^n$ dominates, increasing $\mathcal{G}_{tot}$ amplifies signal and noise identically and the SNR saturates towards $\sqrt{S_{VV}^s/S_{VV}^n}$. Finally, at high pump power, the backaction contribution increases (with $S_{FF}^{ba} \propto n$), so that the SNR generally exhibits an optimum as a function of $n$ [36,40].

## 4. Total transduction gain and ultimate sensitivity of the transducer

To illustrate the potential of such a transducer, we compute the total gain and the thermal noise limited sensitivity in the low cooperativity limit $C = 4g_0^2 n/\kappa\Gamma_m \ll 1$, where cavity back-action force noise can be neglected. The total transduction gain at detuning $\Delta = -\Omega_m$ is

$$\mathcal{G}_{tot}(\Omega_m) = \sqrt{\frac{C\kappa_c Z\omega_c}{\kappa\Omega_m m_{eff}\Gamma_m}}|V\partial_x C_{eq}|. \qquad (13)$$

Additionally, the ultimate sensitivity is obtained for an SNR of 1. Assuming that the detection noise $S_{det}$ and the electrical input noise $S_{VV}^n$ can technically be made negligible, we get

$$\sqrt{S_{VV}^{min}} = \frac{\sqrt{2m_{eff}\Gamma_m k_B T}}{|V\partial_x C_{eq}|}. \qquad (14)$$

Let us estimate the gain and sensitivity that could be obtained with state-of-the art sub-systems. To date, highly stressed silicon nitride membrane resonators are the best candidates to perform such an experiment. They can have frequencies around 4 MHz, masses around 1 ng, and they can be thermalized at a temperature of 10 mK in a dilution cryostat [14], exhibiting quality factors of at least 100 million, which leads to $\Gamma_m/2\pi$ smaller than 10 mHz. Such extreme quality factors can be obtained through phononic engineering in silicon-nitride stressed structures [18,23,24,35,39,41], relying on dissipation dilution [42]. Finally, sub-micrometer distance can be reached in vacuum gap capacitors [18]. For a 500 nm distance and a surface of $20\,\mu m \times 20\,\mu m$, we find $C_m \simeq 10$ fF, and $\partial_x C_m \approx 15$ nF/m. We assume that $C_b$ is large enough such that $\eta \simeq 1$. We also assume a maximum dc bias of 50 V: while cryostat dc lines and electronic components can typically handle up to 150 V, avalanche breakdown in semiconducting substrates

usually imposes a lower practical limit [14,43]. In this configuration, assuming a cooperativity of $C = 0.1$, $\kappa_c/2\pi = 0.5$ MHz, and $\kappa_i/2\pi = 1$ MHz, the total gain would be $\mathcal{G}_{\text{tot}}(\Omega_{\text{m}}) = 44$ dB, and the minimum voltage modulation that could be detected is of the order of 200 fV/$\sqrt{\text{Hz}}$, or 10 ne/$\sqrt{\text{Hz}}$ in terms of charge modulation, rivaling with the lowest sensitivities reported so far [8,9,12,13].

## 5. Experimental implementation

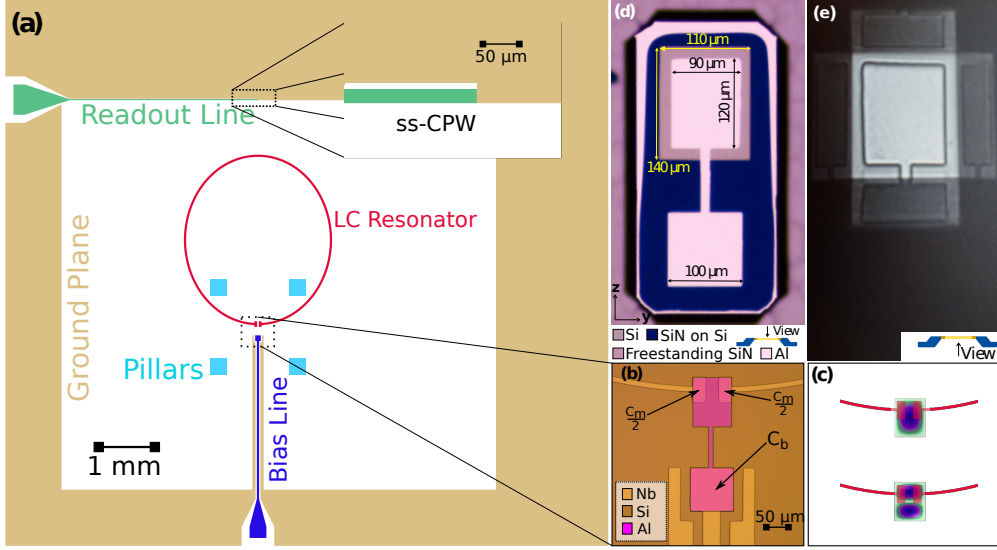In this section, we demonstrate an experimental implementation of such an rf-to-microwave transducer.



**Figure 2.** (a) LC resonator chip design: LC resonator (red), biasing line (blue), the read-out line (green), the ground plane (gold), and the aluminum pillars (light blue) used as spacers in the flip-chip process. For visualization, the inductor track (width: 8 µm) has been thickened. Inset: Close-up on the read-out line which is a single-sided coplanar waveguide terminating into the ground plane. (b) Optical microscope image of the capacitor pads of the LC resonator, overlaid with the membrane electrodes (pink). (c) The LC resonator (red) overlaid with simulated mode profiles of the first to membrane modes 11 and 12. (d) Optical microscope image of the membrane sample, standing on a rectangular pedestal 25 µm above the silicon substrate. The pedestal with the membrane and electrodes is in focus, the substrate is not in focus. (e) Optical microscope image of the membrane sample, seen from the other side. The released metalized SiN membrane can be seen at the top. Mirror images on the four edges of the membrane come from the smooth inclined silicon crystalline planes obtained after etching with KOH trough the substrate. Figures (d) and (e) are taken from [14].

### 5.1. *Membrane oscillator*

The mechanical oscillator is a 90 nm-thick, high-stress ($\sigma \simeq 1$ GPa) Silicon Nitride (SiN) rectangular membrane with dimensions $l_y = 110$ µm, and $l_z = 140$ µm. The combination of high tensile stress and low thickness yields high quality factors thanks to dissipation dilution [42]. The central part of the membrane (rectangle of dimensions 90 µm × 120 µm) is coated with a 30 nm-thick aluminum layer, leaving a narrow uncoated stripline at the edges. The aluminum biasing circuit consists of a square aluminum pad of 100 µm side length, forming one electrode of $C_{\text{b}}$, that is electrically connected to the membrane pad with a thin stripline. A schematic of this layout is shown in Figure 2.

The fabrication process is the following. A silicon wafer is coated on both sides with a (LPCVD) 100 nm SiN layer, and is annealed at 1100 °C [44] for four hours. The membranes are released by wet etching at 85 °C in a 30 % KOH solution, after performing an optical lithography step [14,45,46] on one side of the wafer. Additionally, a second optical lithography step followed by KOH etching on the other side of the wafer (the membrane side) defines a 25 μm-deep recess over the entire chip except the membrane and dc bias circuit footprint (Figure 2(d)). The resulting relief maintains a generous inter-chip spacing everywhere outside the active membrane region, so that in the final assembly, any dust particles trapped there cannot affect the capacitor gap beneath the membrane. The membranes are dipped in a 10 % diluted HF solution to remove any dirt and debris. During this step, HF etches 10 nm of SiN in total, leaving a 90 nm-thick membrane. The dc biasing electrodes are fabricated out of aluminum using a lift-off process.

The mechanical modes frequencies, profiles, and quality factors were characterized at room temperature in an optical interferometer prior to metalization, and show frequencies of 3.22 MHz (mode 11) and 4.73 MHz (mode 12), in good agreement with the result expected from the plate theory [47] $\Omega_{pq} = \pi \sqrt{(\sigma/\rho)(p^2/l_y^2 + q^2/l_z^2)}$, with $p$ and $q$ being the integer mode indices, $\rho$ the membrane density. Finally, mechanical quality factors were measured near $6 \times 10^4$ prior to aluminum metalization.

## 5.2. *LC resonator*

The LC resonator capacitor is made of two rectangular pads (size 60 μm × 90 μm) designed such that the microwave mode couples primarily to the first two membrane modes (modes 11 and 12 on Figure 2(c)). They are connected to a nearly circular ring inductor. The LC resonator chip also hosts a 100 μm × 100 μm metal pad forming one electrode of $C_b$. Figure 2(a)–(b) shows the biasing pad and the biasing line (blue in (a)), the membrane electrode, the inductor, and their alignment with the membrane chip. On the side opposite to the capacitor electrodes, the inductor couples to a single-sided coplanar waveguide read-out line, impedance-matched to 50 Ω (see Figure 2(a) and inset). Finite-element simulations with Ansys HFSS are used to optimize the circuit geometry. A gap-to-track ratio of 4/15 yields a 50 Ω characteristic impedance, matching that of the external line. The simulations are also used to set the fundamental resonance at $\omega_c/2\pi = 7$ GHz and to adjust the mutual inductance between the coplanar waveguide and the LC resonator. The superconducting circuit is fabricated by sputtering a niobium film onto an intrinsic silicon wafer, then patterning the film with optical lithography, followed by reactive-ion etching.

## 5.3. *Flip-chip assembly*

Capacitive coupling between the membrane and the LC resonator, is obtained via a flip-chip assembly technique [39,48]. The membrane and circuit electrodes are brought in close proximity, forming the vacuum gap capacitors $C_b$ (bias-to-membrane) and $C_m$ (membrane-to-LC circuit). The chip distance is set by four 600-nm aluminum spacers, evaporated on the LC resonator chip. The assembly is performed on an MJB4 mask aligner using a custom-designed mask holder, used to pick up the membrane chip and align it on top of the LC resonator chip (see Figure 3). Prior to alignment, the LC resonator chip has been glued inside a microwave-shielding box (Joint Assembly for the Wiring of Superconducting circuits [49]), in which the various required rf, microwave and dc ports are wirebonded to macroscopic connectors (see Figure 3). A viewing hole in the holder provides top-down visibility of the membrane. Once aligned, the two chips are glued together in place using Dymax OP-67-LC UV-curing adhesive.

The LC resonator frequency is measured at $\omega_c/2\pi = 7.04$ GHz before flip-chip and $\omega_c/2\pi = 6.21$ GHz after flip-chip, from which we estimate the participation ratio of the vacuum-gap
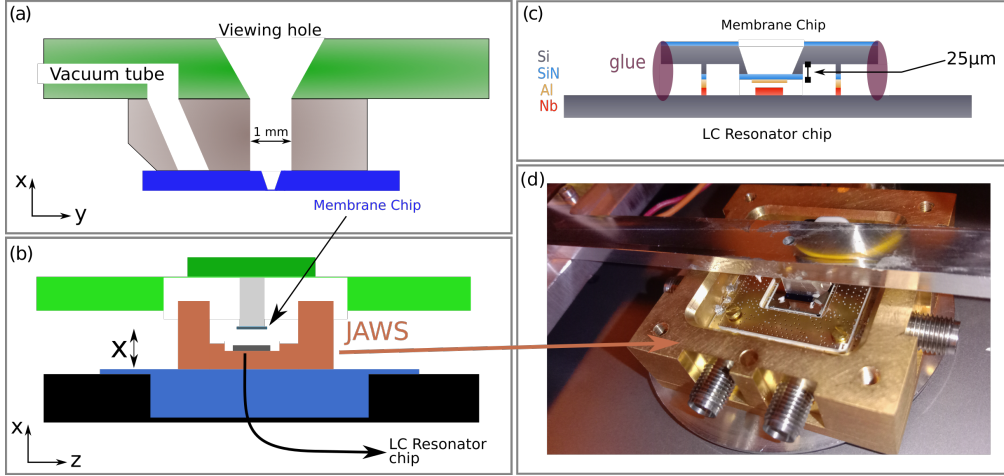
**Figure 3.** (a) Illustration of the custom mask holder used in the flip-chip process, showing the membrane chip (blue) being picked up via a vacuum suction tube. A viewing hole allows visual alignment. (b) We use the 3 axis micropositioning of the MJB4 mask aligner system under binocular microscope to align the membrane chip with the LC resonator chip that is already wirebonded in a microwave shielding box, and bring them in contact. (c) Cross-sectional schematic of the final device. The membrane pedestal at a distance of 25 μm from the substrate can be seen in the center. On the LC resonator chip, the 600 nm-tall aluminum pillars (not to scale) are used as spacers to set the inter-chip distance. Glue drops are also shown at the chip edges. (d) Photograph of the completed flip-chip assembly in the mask aligner, with chips glued together (white drops indicate adhesive). The microwave-shielding box is indicated.

capacitor $C_{\mathrm{m}}/(C_{\mathrm{m}}+4C_{\mathrm{s}}) \sim 0.22$. The measured linewidths are respectively $\kappa/2\pi \approx 1.6$ MHz and $\kappa/2\pi \approx 1.34$ MHz before and after the flip-chip process, ensuring that the system operates in the resolved sideband regime.

## 5.4. *Electromechanical characterization of mechanical modes*

The mechanical mode is probed by sending a microwave tone at $\omega_{\mathrm{d}} = \omega_{\mathrm{c}} - \Omega_{\mathrm{m}}^{pq}$ on the read-out port ($pq$ stand for the mechanical mode indices: 11 and 12), and monitoring the mechanical sideband on the reflected signal with a vector signal analyzer (VSA). A comprehensive cryostat wiring schematic can be found in the supplementary material. An example of a VSA trace is shown in Figure 4(a). Sideband spectra are plotted versus $V$, in Figure 4(b)–(c) for the two mechanical modes. We observe the expected anti-spring effect, and a linewidth increase by a factor $\lesssim 2$ between 0 and 49 V bias, which we attribute to heating via Joule effect. Analyzing this parabolic dependence reveals a membrane-LC resonator distance near 1.5 μm, and zero bias frequencies of 2.4 MHz and 3.6 MHz for the modes 11 and 12 respectively — the values having been shifted due to the added mass of aluminum. In Figure 4(d)–(e), we show the mechanical mode amplitude versus time after resonant drive excitation through the rf port. Fitting an exponential decay to the data yields the decay rates $\Gamma_{\mathrm{m}}^{11}/2\pi = 89$ Hz and $\Gamma_{\mathrm{m}}^{12}/2\pi = 16$ Hz. Note however, that in experiments performed in this work, a microwave pump power of $-30$ dBm results in a small cold damping effect [36]. The measured modified decay rates are $\Gamma_{\mathrm{em}}^{11}/2\pi = 114$ Hz and $\Gamma_{\mathrm{em}}^{12}/2\pi = 24$ Hz. Finally, we use a standard calibration method [50] to extract $g_0^{11}/2\pi = 0.29 \pm 0.07$ Hz and $g_0^{12}/2\pi = 0.23 \pm 0.05$ Hz. At $-30$ dBm microwave pump power, chosen as the highest pump power compatible with stable cryostat temperature, it yields cooperativities of 0.28 and 0.5 for the modes 11 and 12, respectively, and provides the ratio between the two modes effective masses. To obtain an absolute value of the effective masses, we proceed in two
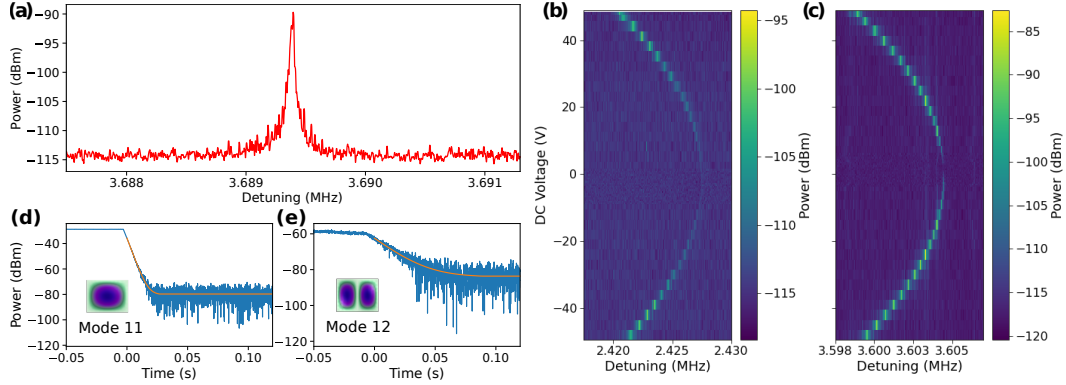
**Figure 4.** (a) Sideband noise amplitude from mode 12, on the read-out reflected signal, with the microwave pump at $\omega_d = \omega_c - \Omega_m$, and with a non zero dc bias $V = 30$ V. (b) and (c) show the frequency shift of the two mechanical modes for $V \in [-49, 49]$ V, highlighting the anti-spring effect. (d) and (e): Ring-down measurements for mode 11 and 12 performed at 10 mK near zero dc bias. The membrane mode is driven by a strong resonant rf tone through the biasing line, and its exponentially decaying amplitude after turning off the rf tone, is monitored versus time. By fitting the decay with an exponential curve (yellow line) we extract $\Gamma_m$.

steps. First, for a stress-dominated rectangular membrane the motional mass is one quarter of the physical mass, a result that is independent of the mode indices [35]. Second, only the electrode area contributes to the signal, such that the motional mass must be multiplied by a read-out dilution factor, equal to the ratio of the squared mode amplitude integrated over the electrodes area, to that over the entire membrane. Defining the displacement coordinate as the maximum transverse amplitude, we find $m_{\text{eff}}^{11} = 6.25$ ng and $m_{\text{eff}}^{12} = 4.27$ ng, which is compatible with the measured mass ratio.

## 5.5. *Mechanical modes thermalization and electrical noise transduction*

The mechanical sideband area can be obtained by integrating Eq. (1). We find

$$\mathcal{A}_V = \frac{1}{m_{\text{eff}}\Omega_m^2(V)}\left(k_B T \frac{\Gamma_m}{\Gamma_{\text{em}}} + \frac{S_{VV}^n}{m_{\text{eff}}\Gamma_{\text{em}}}(\partial_x C_{\text{eq}})^2 (V - V_0)^2\right). \tag{15}$$

The first term in the right-hand side gives the standard linear dependence with temperature. The second term in the rhs is the parabolic dependence of the mechanical energy due to transduced electrical noise. Here the offset $V_0$ accounts for any trapped charge on the floating superconducting island. Scanning the cryostat temperature from 10 mK to 500 mK when the effective bias voltage is set to zero reveals the linear dependence of the peak area with temperature as shown in Figure 5 (left column) for both modes, confirming that the membrane modes are thermalized to the cryostat base-temperature. Additionally, in Figure 5 (right column), we plot the sideband area versus bias voltage. Eq. (15) is fitted to the data obtained at 10 mK and 500 mK, emphasizing the validity of our model.

## 5.6. *SNR of transduction experiment*

At a non zero bias voltage, we sweep the frequency $\Omega_{\text{rf}}$ of a sinusoidal rf drive across the mechanical mode frequency. The sideband spectra are shown in Figure 6(a) and (d) at various detuning $\Omega_{\text{rf}} - \Omega_m$. As predicted by Eq. (11), we observe an overall Lorentzian envelope stemming from the mechanical susceptibility. The noise spectra obtained in the absence of rf signal appears
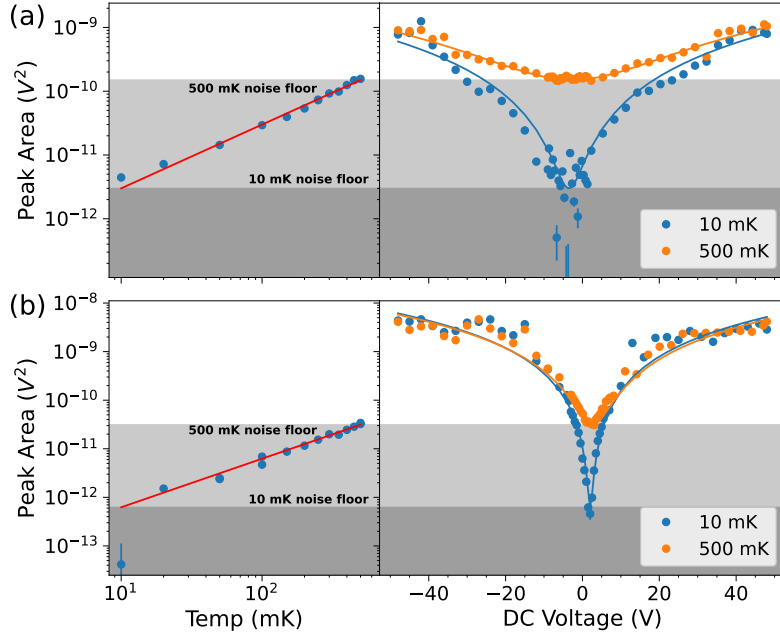
**Figure 5.** Membrane modes thermalization and electrical noise transduction. Left column: Transduced side-band spectrum area versus cryostat temperature at zero bias voltage. (a): Mode 11. (b): Mode 12. From a linear fit (red), we extract a slope of $3.57 \times 10^{-10}$ $V^2$/K for mode 11, shown in (a), and $9.8 \times 10^{-11}$ $V^2$/K for mode 12, after correcting for power broadening. The 10 mK area value and 500 mK area value of each mode define the corresponding thermal noise floor highlighted in two different gray colors. Right column: Area versus $V$ at two different temperatures. Eq. (15) is fitted to the data (solid lines).

in red in Figure 6(a) and (d). By monitoring the height of the transduced sideband spectrum on resonance, when $\Omega_{rf} = \Omega_m$, across the voltage range of $-49$ V to 49 V, and after normalizing with the resolution bandwidth of the VSA, we extract the signal to noise ratio of the transduction experiment, as defined by Eq. (12). The results are shown in Figure 6(b) and (e). The data reveal a linear dependence at small $V$, followed by a saturation, when entering in the regime where the transduced electrical noise dominates other noise contributions (detection and thermal noises). For mode 11, only the linear regime is accessible. For mode 12, the lower values of thermal noise and detector noise yields a factor $\sim 2$ steeper slope in the linear regime, sufficient to reach a saturation due to electrical noise.

To analyze the data we first rewrite Eq. (12)

$$\mathrm{SNR}^2 = \frac{|V\partial_x C_{eq}|^2 S_{VV}^s}{|V\partial_x C_{eq}|^2 S_{VV}^n + S_{FF}^{th} + S_{FF}^{ba} + S_{FF}^{det}}, \tag{16}$$

where we have defined the equivalent force noise associated to detector noise $S_{FF}^{det} = S_{det}/\left(\mathcal{G}_{em}^2(\omega)\left|\chi_m(\omega, V)\right|^2\right)$. The term $S_{FF}^{th} + S_{FF}^{ba}$ is computed from Eq. (10), after substituting $\Gamma_m$ with $\Gamma_{em}$ to account for backaction. $S_{FF}^{det}$ is then obtained experimentally from the noise spectra measured at zero effective dc voltage (spectra used to compute the area points in the left column of Figure 5). More precisely, we compute the ratio $(S_{FF}^{th} + S_{FF}^{det} + S_{FF}^{ba})/S_{FF}^{det}$ between the noise peak maximum and the noise floor away from the resonance. Using the computed value of $S_{FF}^{th} + S_{FF}^{ba}$ then yields $S_{FF}^{det}$. Next, we evaluate $|\partial_x C_{eq}|$ by using geometrical parameters. Finally, fitting Eq. (16) to the data, provides the values of $S_{VV}^s[\Omega_m]$ and $S_{VV}^n$, which is assumed locally frequency-independent. We find $S_{VV}^s[\Omega_m] = -70.4$ dBm for mode 11 and $-70.3$ dBm for
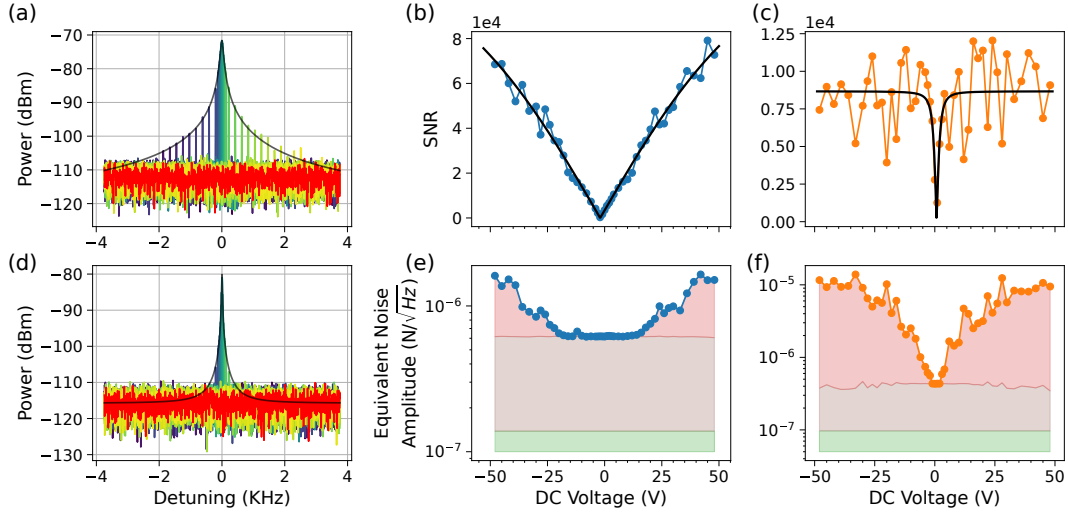
**Figure 6.** Rf signal transduction experiment for mode 11 in (a) and mode 12 in (d). An rf tone is applied on the bias-line, and its frequency is swept through the mechanical mode resonance, while maintaining $V$ close to zero. The LC Resonator is probed via the read-out line like in previous experiments. The VSA traces, taken at various detuning $(\Omega_{rf}-\Omega_m)/2\pi$, are shown with a gradient of colors from blue to green. The transduction envelope reveals the membrane mode susceptibility, and can be fitted with a Lorentzian curve (black solid line). The red curve shows the VSA trace in absence of rf signal. (b) and (e) show the measured Signal to Noise Ratio (SNR) of the rf peaks on resonance, transduced by the membrane modes 11 and 12 respectively, with the dc bias varying from $-49$ V to $49$ V, and with an rf drive of power $-70$ dBm. (c) and (f) respectively highlight the overall force noise budget: the gray-filled area represents the detector noise, green-filled area the thermal noise, and the red-filled area shows the transduced electrical noise, in the data of (b) and (e).

mode 12, in good agreement with the rf drive power of $-70$ dBm — estimated from the source power and the total attenuation of the rf line — confirming the distance value obtained from anti-spring effect. The value of $S_{VV}^n(\Omega_m)$ is calculated only in the case of mode 12, for which the SNR saturation is reached. We find $\sqrt{S_{VV}^n(\Omega_m^{12})} = 7.8$ nV/$\sqrt{\text{Hz}}$. Finally, in Figure 6(e)–(f), we show the various noise contributions versus dc voltage: thermal and cavity backaction noise, detection noise, transduced electrical noise. Note, that in our present setup the cooperativity remains $C \lesssim 1$, and the detected background is dominated by amplification-chain added noise downstream of the device. Since this contribution does not enter the cavity, it does not generate imprecision-backaction correlations; we therefore neglect correlation terms in the analysis. Note, that if the dominant noise were incident on the cavity field (e.g., pump technical noise), correlations could impact the signal [18,40,51,52].

### 5.7. *Electrometer sensitivity*

To evaluate the sensitivity of this electrometer, we determine the signal at which the SNR at maximum dc bias reaches 1. In practice, it is obtained by dividing the signal strength $S_{VV}^s$ by the highest measured SNR (value taken from the fit). The voltage and charge sensitivities for mode 11 and 12 are listed in Table 1. Note that the sensitivity of mode 11 is limited by the maximal dc voltage value that can be reached in the experiment, whereas the sensitivity of mode 12 is limited by electrical noise. Our interpretation is that electrical noise might be significantly different at the two mode frequencies.

**Table 1.** Maximum SNR, measured and ideal sensitivity values for the two modes. The values are obtained at $-30$ dBm microwave pump power, and $-70$ dBm RF tone power. The values in elementary charge per root Hertz are calculated from the biasing circuit capacitance $C_{\text{eq}} \approx 15$ fF. The ideal sensitivity is the thermal noise limited sensitivity. All sensitivity values and maximum SNR are calculated/measured at 49 V, and $\Gamma_{\text{m}}$ values are recalled in the last column.

| Mode | Max SNR | Measured sensitivity | | Ideal sensitivity | | $\Gamma_{\text{m}}/2\pi$ |
|------|---------|---------------------|---------------------|-------------------|-------------------|------|
|      |         | $(\text{nV}/\sqrt{\text{Hz}})$ | $(\mu\text{e}/\sqrt{\text{Hz}})$ | $(\text{nV}/\sqrt{\text{Hz}})$ | $(\mu\text{e}/\sqrt{\text{Hz}})$ | (Hz) |
| 1 | 96 dB | 0.9 | 87 | 0.1 | 9 | 89 |
| 2 | 78 dB | 7.8 | 760 | 0.05 | 5 | 16 |

## 6. Conclusion

We have presented a dc-biased membrane-in-LC architecture that performs heterodyne conversion of radio-frequency voltages to the microwave band, while acting as a sensitive electrometer. By decoupling the total gain from microwave pump power through electrostatic pre-amplification, we avoid the excess shot noise and heating that constrain conventional cavity converters, at the cost of adding electrical noise, which can however be mitigated by better filtering strategies, or using symmetry protection [14]. In a flip-chip device with a 1.5 μm vacuum gap, we observe the expected anti-spring tuning effect on the mechanical modes, and achieve a charge sensitivity of 87 μe/$\sqrt{\text{Hz}}$ (0.9 nV/$\sqrt{\text{Hz}}$). By implementing a related concept at 10 mK (rather than room temperature) and with a microwave (rather than optical) read-out, our device improves the voltage sensitivity by roughly three orders of magnitude compared with the rf-to-optical transducer of Bagci et al. [28], while delivering an output that is natively compatible with quantum microwave circuitry.

Crucially, the heterodyne mixing of the RF signal with a GHz local oscillator inside the cryogenic cavity bypasses the large Johnson noise of conventional MHz-band amplifiers. The remaining imprecision is set by the noise temperature of the microwave HEMT, operating well below the room-temperature limit. This inherent noise advantage, combined with electrostatic pre-amplification, enables high-sensitivity detection inaccessible to direct rf measurement.

Straightforward improvements would push performance further: shortening the vacuum gap to sub-micrometer dimensions, as demonstrated in [18], and adopting ultracoherent $Si_3N_4$ drums with $Q > 10^8$ [24,35,39] would enhance the electrostatic lever arm by an order of magnitude while suppressing thermal force noise by 20–30 dB. Phononic-crystal defect regions can be engineered with lateral dimensions larger than 200 μm range [53,54], and can be functionalized with a metalized (Al) pad that is flip-chip coupled to superconducting capacitor electrodes [18,39]. Our model predicts these advances would yield 44 dB total gain and voltage sensitivity below 200 fV/$\sqrt{\text{Hz}}$ — rivaling state-of-the-art cryogenic electrometers.

## Declaration of interests

The authors do not work for, advise, own shares in, or receive funds from any organization that could benefit from this article, and have declared no affiliations other than their research organizations.

## Supplementary material

Supporting information for this article is available on the journal's website under https://doi.org/10.5802/crphys.273 or from the authors.

## References

[1] R. G. Knobel and A. N. Cleland, "Nanometre-scale displacement sensing using a single electron transistor", *Nature* **424** (2003), no. 6946, pp. 291–293.

[2] R. J. Schoelkopf, P. Wahlgren, A. A. Kozhevnikov, P. Delsing and D. E. Prober, "The radio-frequency single-electron transistor (RF-SET): A fast and ultrasensitive electrometer", *Science* **280** (1998), no. 5367, pp. 1238–1242.

[3] M. P. Blencowe and M. N. Wybourne, "Sensitivity of a micromechanical displacement detector based on the radio-frequency single-electron transistor", *Appl. Phys. Lett.* **77** (2000), no. 23, pp. 3845–3847.

[4] H. Brenning, S. Kafanov, T. Duty, S. Kubatkin and P. Delsing, "An ultrasensitive radio-frequency single-electron transistor working up to 4.2 K", *J. Appl. Phys.* **100** (2006), no. 11, article no. 114321.

[5] A. Aassime, D. Gunnarsson, K. Bladh, P. Delsing and R. J. Schoelkopf, "Radio-frequency single-electron transistor: Toward the shot-noise limit", *Appl. Phys. Lett.* **79** (2001), no. 24, pp. 4031–4033.

[6] S. J. Angus, A. J. Ferguson, A. S. Dzurak and R. G. Clark, "A silicon radio-frequency single electron transistor", *Appl. Phys. Lett.* **92** (2008), no. 11, article no. 112103.

[7] A. N. Korotkov and M. A. Paalanen, "Charge sensitivity of radio frequency single-electron transistor", *Appl. Phys. Lett.* **74** (1999), no. 26, pp. 4052–4054.

[8] M. C. Cassidy, A. S. Dzurak, R. G. Clark, K. D. Petersson, I. Farrer, D. A. Ritchie and C. G. Smith, "Single shot charge detection using a radio-frequency quantum point contact", *Appl. Phys. Lett.* **91** (2007), no. 22, article no. 222104.

[9] J. J. Viennot, M. R. Delbecq, M. C. Dartiailh, A. Cottet and T. Kontos, "Out-of-equilibrium charge dynamics in a hybrid circuit quantum electrodynamics architecture", *Phys. Rev. B* **89** (2014), article no. 165404 (4 pages).

[10] W. Lu, Z. Ji, L. Pfeiffer, K. West and A. J. Rimberg, "Real-time detection of electron tunnelling in a quantum dot", *Nature* **423** (2003), no. 6938, pp. 422–425.

[11] C. Volk, A. Chatterjee, F. Ansaloni, C. M. Marcus and F. Kuemmeth, "Fast Charge Sensing of Si/SiGe Quantum Dots via a High-Frequency Accumulation Gate", *Nano Lett.* **19** (2019), no. 8, pp. 5628–5633.

[12] M. F. Gonzalez-Zalba, S. Barraud, A. J. Ferguson and A. C. Betz, "Probing the limits of gate-based charge sensing", *Nat. Commun.* **6** (2015), no. 1, article no. 6084 (8 pages).

[13] B.-L. Najera-Santos, R. Rousseau, K. Gerashchenko, et al., "High-Sensitivity ac-Charge Detection with a MHz-Frequency Fluxonium Qubit", *Phys. Rev. X* **14** (2024), no. 1, article no. 011007 (18 pages).

[14] K. Gerashchenko, R. Rousseau, L. Balembois, et al., "Probing the quantum motion of a macroscopic mechanical oscillator with a radio-frequency superconducting qubit", preprint, 2025. Online at https://arxiv.org/abs/2505.21481.

[15] T. Faust, P. Krenn, S. Manus, J. P. Kotthaus and E. M. Weig, "Microwave Cavity-Enhanced Transduction for Plug-and-Play Nanomechanics at Room Temperature", *Nat. Commun.* **3** (2012), article no. 728 (6 pages).

[16] J. D. Teufel, T. Donner, D. Li, et al., "Sideband cooling of micromechanical motion to the quantum ground state", *Nature* **475** (2011), no. 7356, pp. 359–363.

[17] T. Rocheleau, T. Ndukum, C. Macklin, J. Hertzberg, A. A. Clerk and K. Schwab, "Preparation and detection of a mechanical resonator near the ground state of motion", *Nature* **463** (2010), no. 7277, pp. 72–75.

[18] Y. Seis, T. Capelle, E. C. Langman, S. Saarinen, E. Planz and A. Schliesser, "Ground state cooling of an ultracoherent electromechanical system", *Nat. Commun.* **13** (2022), no. 1, article no. 1507 (7 pages).

[19] J. Chan, T. P. M. Alegre, A. H. Safavi-Naeini, J. T. Hill, A. Krause, S. Gröblacher, M. Aspelmeyer and O. Painter, "Laser cooling of a nanomechanical oscillator into its quantum ground state", *Nature* **478** (2011), no. 7367, pp. 89–92.

[20] M. Rossi, D. Mason, J. Chen, Y. Tsaturyan and A. Schliesser, "Measurement-based quantum control of mechanical motion", *Nature* **563** (2018), no. 7729, pp. 53–58.

[21] R. W. Peterson, T. P. Purdy, N. S. Kampel, R. W. Andrews, P.-L. Yu, K. W. Lehnert and C. A. Regal, "Laser cooling of a micromechanical membrane to the quantum backaction limit", *Phys. Rev. Lett.* **116** (2016), no. 6, article no. 063601.

[22] L. Qiu, I. Shomroni, P. Seidler and T. J. Kippenberg, "Laser cooling of a nanomechanical oscillator to its zero-point energy", *Phys. Rev. Lett.* **124** (2020), no. 17, article no. 173601 (7 pages).

[23] A. Cupertino, D. Shin, L. Guo, P. G. Steeneken, M. A. Bessa and R. A. Norte, "Centimeter-scale nanomechanical resonators with low dissipation", *Nat. Commun.* **15** (2024), no. 1, article no. 4255 (10 pages).

[24] M. J. Bereyhi, A. Arabmoheghi, A. Beccari, S. A. Fedorov, G. Huang, T. J. Kippenberg and N. J. Engelsen, "Perimeter modes of nanomechanical resonators exhibit quality factors exceeding 10 9 at room temperature", *Phys. Rev. X* **12** (2022), no. 2, article no. 021036 (19 pages).

[25] A. H. Ghadimi, S. A. Fedorov, N. J. Engelsen, M. J. Bereyhi, R. Schilling, D. J. Wilson and T. J. Kippenberg, "Elastic strain engineering for ultralow mechanical dissipation", *Science* **360** (2018), no. 6390, pp. 764–768.

[26] R. W. Andrews, R. W. Peterson, T. P. Purdy, K. Cicak, R. W. Simmonds, C. A. Regal and K. W. Lehnert, "Bidirectional and Efficient Conversion between Microwave and Optical Light", *Nat. Phys.* **10** (2014), no. 4, pp. 321–326.

[27] A. P. Higginbotham, P. S. Burns, M. D. Urmey, et al., "Harnessing electro-optic correlations in an efficient mechanical converter", *Nat. Phys.* **14** (2018), no. 10, pp. 1038–1042.

[28] T. Bagci, A. Simonsen, S. Schmid, et al., "Optical detection of radio waves through a nanomechanical transducer", *Nature* **507** (2014), no. 7490, pp. 81–85.

[29] M. Forsch, R. Stockill, A. Wallucks, I. Marinković, C. Gärtner, R. A. Norte, A. Fiore and S. Gröblacher, "Microwave-to-Optics Conversion Using a Mechanical Oscillator in Its Quantum Ground State", *Nat. Phys.* **16** (2020), pp. 69–74.

[30] M. Mirhosseini, A. Sipahigil, M. Kalaee and O. Painter, "Superconducting Quantum Electromechanics Interface for Microwave-to-Optical Conversion", *Nature* **588** (2020), pp. 599–603.

[31] Q. Unterreithmeier, E. M. Weig and J. P. Kotthaus, "Universal transduction scheme for nanomechanical systems based on dielectric forces", *Nature* **458** (2009), pp. 1001–1004.

[32] J. J. Viennot, X. Ma and K. W. Lehnert, "Phonon-number-sensitive electromechanics", *Phys. Rev. Lett.* **121** (2018), no. 18, article no. 183601 (6 pages).

[33] I. Moaddel Haghighi, N. Malossi, R. Natali, G. Di Giuseppe and D. Vitali, "Sensitivity-bandwidth limit in a multi-mode opto-electro-mechanical transducer", *Phys. Rev. Appl.* **9** (2018), article no. 034031 (15 pages).

[34] M. Bonaldi, A. Borrielli, G. Di Giuseppe, et al., "Low Noise Opto-Electro-Mechanical Modulator for RF-to-Optical Transduction in Quantum Communications", *Entropy* **25** (2023), no. 7, article no. 1087 (14 pages).

[35] Y. Tsaturyan, A. Barg, E. S. Polzik and A. Schliesser, "Ultracoherent nanomechanical resonators via soft clamping and dissipation dilution", *Nat. Nanotechnol.* **12** (2017), no. 8, pp. 776–783.

[36] M. Aspelmeyer, T. J. Kippenberg and F. Marquardt, "Cavity optomechanics", *Rev. Mod. Phys.* **86** (2014), no. 4, pp. 1391–1452.

[37] J. M. Pate, L. A. Martinez, J. J. Thompson, R. Y. Chiao and J. E. Sharping, "Electrostatic tuning of mechanical and microwave resonances in 3D superconducting radio frequency cavities", *AIP Adv.* **8** (2018), no. 11, article no. 115223 (7 pages).

[38] X. Zhou, S. Venkatachalam, R. Zhou, H. Xu, A. Pokharel, A. Fefferman, M. Zaknoune and E. Collin, "High-Q Silicon Nitride Drum Resonators Strongly Coupled to Gates", *Nano Lett.* **21** (2021), no. 13, pp. 5738–5744.

[39] H. Patange, *RF Transduction in a DC-Biased Superconducting Electromechanical System*, Sorbonne Université (France), 2025.

[40] X. Zhou, D. Cattiaux, D. Theron and E. Collin, "Electric circuit model of microwave optomechanics", *J. Appl. Phys.* **129** (2021), no. 11, article no. 114502.

[41] P.-L. Yu, K. Cicak, N. S. Kampel, Y. Tsaturyan, T. P. Purdy, R. W. Simmonds and C. A. Regal, "A phononic bandgap shield for high-Q membrane microresonators", *Appl. Phys. Lett.* **104** (2014), no. 2, article no. 023510.

[42] S. A. Fedorov, N. J. Engelsen, A. H. Ghadimi, M. J. Bereyhi, R. Schilling, D. J. Wilson and T. J. Kippenberg, "Generalized dissipation dilution in strained mechanical resonators", *Phys. Rev. B* **99** (2019), no. 5, article no. 054107 (8 pages).

[43] S. M. Sze, M.-K. Lee and M.-K. Lee, *Semiconductor devices, physics and technology*, 3. ed edition, John Wiley & Sons, 2012.

[44] S. Mittal, K. Adachi, N. E. Frattini, et al., "Annealing reduces Si 3 N 4 microwave-frequency dielectric loss in superconducting resonators", *Phys. Rev. Appl.* **21** (2024), no. 5, article no. 054044 (12 pages).

[45] E. Ivanov, T. Capelle, M. Rosticher, et al., "Edge mode engineering for optimal ultracoherent silicon nitride membranes", *Appl. Phys. Lett.* **117** (2020), no. 25, article no. 254102.

[46] E. Ivanov, T. Capelle, M. Rosticher, et al., *Edge mode engineering for optimal ultracoherent SiN membrane designs*, dataset, Zenodo, v1, 2020. Online at https://zenodo.org/records/4055087.

[47] A. W. Leissa, *Vibration of plates*, special publication, NASA, no. NASA-SP-160, 1969.

[48] T. Capelle, *Electromechanical cooling and parametric amplification of an ultrahigh-Q mechanical oscillator*, Sorbonne Université (France), 2020.

[49] M. Villiers, *Dynamically Enhancing Qubit-Photon Interactions with Anti-Squeezing*, Sorbonne Université (France), 2023.

[50] M. L. Gorodetksy, A. Schliesser, G. Anetsberger, S. Deleglise and T. J. Kippenberg, "Determination of the vacuum optomechanical coupling rate using frequency noise calibration", *Opt. Express* **18** (2010), no. 22, pp. 23236–23246.

[51] A. H. Safavi-Naeini, J. Chan, J. T. Hill, S. Gröblacher, H. Miao, Y. Chen, M. Aspelmeyer and O. Painter, "Laser noise in cavity-optomechanical cooling and thermometry", *New J. Phys.* **15** (2013), no. 3, article no. 035007 (35 pages).

[52] V. Sudhir, D. J. Wilson, R. Schilling, H. Schütz, S. A. Fedorov, A. H. Ghadimi, A. Nunnenkamp and T. J. Kippenberg, "Appearance and Disappearance of Quantum Correlations in Measurement-Based Feedback Control of a Mechanical Oscillator", *Phys. Rev. X* **7** (2017), article no. 011001 (14 pages).

[53] E. Planz, X. Xi, T. Capelle, E. C. Langman and A. Schliesser, "Membrane-in-the-middle optomechanics with a soft-clamped membrane at milliKelvin temperatures", *Opt. Express* **31** (2023), no. 25, pp. 41773–41782.

[54] G. Enzian, Z. Wang, A. Simonsen, et al., "Phononically shielded photonic-crystal mirror membranes for cavity quantum optomechanics", *Opt. Express* **31** (2023), no. 8, pp. 13040–13052.